doi.org/10.26434/chemrxiv.9929684.v1

3D Texturing of the Water–Air Interface by Biomimetic Self-Assembly

Erik Bergendal, Richard A. Campbell, Georgia A. Pilkington, Peter Müller-Buschbaum, Mark W. Rutland

Submitted date: 02/10/2019 • Posted date: 04/10/2019

Citation information: Bergendal, Erik; Campbell, Richard A.; Pilkington, Georgia A.; Müller-Buschbaum, Peter; Rutland, Mark W. (2019): 3D Texturing of the Water–Air Interface by Biomimetic Self-Assembly. ChemRxiv. Preprint.

A simple, insoluble monolayer of fatty acid is shown to induce 3D nanotexturing of the water–air interface. This advance has been achieved through the study of monolayers of a methyl-branched long chain fatty acid, analogous to those found on the surface of hair and wool, directly at the water–air interface. Specular neutron reflectometry combined with AFM probing of deposited monolayers shows pronounced 3D surface domains, which are absent for unbranched analogues and which are attributed to hydrocarbon packing constraints. The resulting surface topographies of the water far exceed the height perturbation that can be explained by the presence of capillary waves of a free liquid surface. These have hitherto been considered the only source of perturbation of the flatness of a planar water interface under gravity in the absence of topographical features from the presence of extended, globular or particulate matter. This amounts to a paradigm shift in the study of interfacial films and opens the possibility of 3D texturing of the water–air interface.

3D texturing of the water–air interface by biomimetic self-assembly

Erik Bergendal[1], Richard A. Campbell[2,3], Georgia A. Pilkington[1], Peter Müller-Buschbaum[4,5], Mark W. Rutland[1,6,*]

[1] KTH Royal Institute of Technology, School of Engineering Sciences in Chemistry, Biotechnology and Health, Department of Chemistry, Division of Surface and Corrosion Science, Drottning Kristinas väg 51, 100 44 Stockholm Sweden

[2] Institute Laue-Langevin, 71 avenue des Martyrs, 38042 Grenoble, France

[3] Division of Pharmacy and Optometry, University of Manchester, Manchester M21 9PT, UK.

[4] Physik-Department, Lehrstuhl für Funktionelle Materialen, Technische Universität München, James-Franck-Str.1, 85748 Garching, Germany

[5] Heinz Maier-Leibnitz Zentrum (MLZ), Technische Universität München, Lichtenbergstr. 1, 85748 Garching, Germany

[6] RISE Research Institutes of Sweden, Chemistry, Materials and Surfaces, Box 5607, SE-114 86 Stockholm, Sweden

ABSTRACT

A simple, insoluble monolayer of fatty acid is shown to induce 3D nanotexturing of the water–air interface. This advance has been achieved through the study of monolayers of a methyl-branched long chain fatty acid, analogous to those found on the surface of hair and wool, directly at the water–air interface. Specular neutron reflectometry combined with AFM probing of deposited monolayers shows pronounced 3D surface domains, which are absent for unbranched analogues and which are attributed to hydrocarbon packing constraints. The resulting surface topographies of the water far exceed the height perturbation that can be explained by the presence of capillary waves of a free liquid surface. These have hitherto been considered the only source of perturbation of the flatness of a planar water interface under gravity in the absence of topographical features from the presence of extended, globular or particulate matter. This amounts to a paradigm shift in the study of interfacial films and opens the possibility of 3D texturing of the water–air interface.

In the study of monolayers at the water–air interface, long chain fatty acids have been of interest as model systems for two-dimensional ordering as well as for carboxylic acid–metal ion interactions of biological interest (1–3). The straight chain fatty acid eicosanoic acid (EA, also called arachidic acid) has been the most studied monolayer system due to its simplicity, chain saturation, and subphase insolubility (4–6). The structure and stability of floating and deposited fatty acid monolayers have thus been extensively studied at varying temperature, pH, and subphase composition and concentration (1, 7–10). By far the most common technique to study monolayers at the liquid–air interface is the Langmuir technique (11–13), which allows the study of how surface pressure (derived from surface tension measurement) varies as a function of the area available to the monolayer.

The water–air interface is conventionally considered either as flat (i.e. a planar surface under gravity) or curved (e.g. in bubbles, droplets, and foams). In the former case, various 2D phases of the monolayer (e.g. gaseous, tilted expanded, and untilted expanded) can be inferred from surface pressure–area isotherms, analogous to conventional phase changes with pressure and volume (13, 14), and a surface roughness is imparted from the presence of capillary waves (15, 16). Frequently used complementary techniques for monolayer studies at planar water interfaces are ellipsometry and X-ray scattering (17–19), neutron reflectometry (20, 21), spectroscopy (22, 23), and, indirectly, AFM studies of the films deposited from the water–air interface onto solid substrates. (24, 25).

Formation of 2D surface domains in monolayers, indicating lateral inhomogeneity in the plane of the interface, has been shown for several small molecular weight surfactants (26–31). Domains resolved to date consist of several hundred semi-fluorinated fatty acid or alkane molecules, where deposited monolayers have also been studied with AFM and scattering techniques. The inherent insolubility of the molecules restricts them to a 2D film at the water–air interface, whereas the internal density mismatch imposes both the domain structure and its size. Typically, aside from the roughness originating from the capillary waves, any interfacial topography on a planar water interface under gravity has been assigned only to species present at the interface, such as extended, globular or particular matter in the form of polymer brushes, proteins or nanoparticles, respectively (32–35).

A recent study using non-linear spectroscopy and AFM on the ordering of (unbranched) EA and its *iso*- and *anteiso*-methyl branched derivatives challenged the assumption that the structures at the liquid–air interface are flat, and led to the hypothesis of 3D texturing of the water–air interface itself due to aggregate curvature imposed by tail group packing constraints (36). The unbranched alkyl chains of EA are capable of adopting a uniform, parallel packing, allowing the molecules to form a continuous, flat monolayer on the water surface. The addition of a branch, for example at the *iso* position imposes a packing strain since the maximum packing densities at the two ends of the alkyl chain are different. To maintain optimal packing densities and surface tension, it was proposed (36) that the water–headgroup interface adopted a curvature to accommodate the branch packing, thus locally raising the water interface. This inference, however, was formed indirectly as a result of measurements on deposited films rather than by *in situ* measurements at the water–air interface itself. Thus, the hypothesis remained to be tested directly at the water–air interface. Here, specular neutron reflectometry (NR) at this interface is used to investigate the veracity of the hypothesis and demonstrate how (branched) 19-methyl eicosanoic acid (19-MEA) induces a texturing of the water surface that far exceeds that explicable by the roughness induced by capillary waves. The addition of a methyl branch, such as the one for 19-MEA, is characteristic of the biological molecules forming the outer barrier of hair and wool (37–39), though in that case the branch is at the C18 carbon (18-MEA). 19-MEA was selected in this case since a larger radius of curvature of the aggregates would be expected for interfacial aggregates from a consideration of packing constraints (36), and is thus biomimetic rather than a biomolecule *per se*. To the best knowledge of the authors, this system provides the first *in situ* evidence of 3D ordering of the water–air interface, where only 2D representations or lateral diffraction have previously been invoked (30). This approach will shed light on the possible curvature moderation of biomolecules in the palisade layers of hair and wool (37–39), as well as whether planar water interfaces can be templated against gravity by the combination of surface energy considerations and appropriate choice of self-assembly structures, providing a simple bottom-up approach for 3D nanotexturing.

RESULTS AND DISCUSSION

A verification was performed to demonstrate the existence of ordered domains of the fatty acid under study in this work, 19-MEA, when deposited from the water–air interface onto solid substrates. The depositions were carried out at various surface pressures. Figure S1 in the SI shows examples of such surface pressure–area isotherms. To stabilise and condense the monolayer (7, 9), a pH-buffered salt solution (detailed in Materials and Methods) was used as subphase for all depositions and during NR measurements. AFM imaging of deposited monolayers of 19-MEA onto silicon wafers can be seen in Figure 1, which clearly reveals the formation of domains at all surface pressures. At 0 mN m^{-1} (A) the fatty acids self-assemble into irregular shapes of around 40 nm in diameter. The height of the domains is roughly 25 Å above the silicon substrate, which corresponds well to the theoretical extended chain length of an all-*trans* C_{20} hydrocarbon chain (26.8 Å) (40). At increased surface deposition pressure, the surface is completely covered in domains of more homogenous size distribution, as shown for 10 mN m^{-1} (B) and emphasised by the Fourier transform (FT) inset. At the highest surface pressure of deposition of 40 mN m^{-1} (C), the domains can be seen to be monodisperse and closely packed with hexagonal order. This increased order is clearly reflected in the corresponding FT inset. From the FT and line profiles, the domain size was determined to vary between 40 to 50 nm at 10 mN m^{-1} and close to 50 nm at 40 mN m^{-1}. For comparison, monolayers of the unbranched analogue eicosanoic acid, EA, were also deposited under equivalent conditions. They display a featureless monolayer with no evidence of domain formation (see Figure S2 in SI), in agreement with a wealth of studies on this species (24, 25, 36, 41, 42).

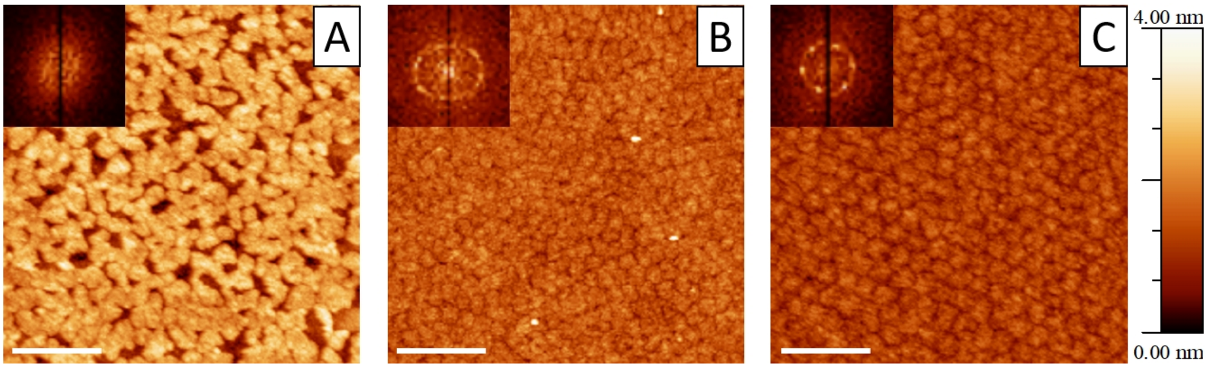

Figure 1. *AFM height images of 19-MEA monolayers deposited on silicon wafers. Depositions were made at surface pressures of (A) 0, (B) 10, and (C) 40 mN m*$^{-1}$*. Self-assembled domains of roughly 40 nm appear already at 0 mN m*$^{-1}$*. FT insets show increasing domain monodispersity. The scalebar represents 200 nm.*

Thus far the observations are consistent with reference 34 and imply a markedly different interfacial packing of the branched and unbranched species, although it cannot be proven that this structure reflects the packing at the water–air interface. To address this issue, neutron reflectometry measurements were performed to directly probe the water–air interface *in situ*. NR profiles of 19-MEA (a) and EA (b) at the water–air interface are shown in Figure 2 as a function of wave vector transfer q_z for several consecutive surface pressures, measured on a single monolayer in each case. With increasing surface pressure, the specular reflectivity for 19-MEA decreases significantly above 0.05 Å^{-1} in q_z. This effect is not seen for EA, where only very small changes in reflectivity are observed with increasing surface pressure. As a reference, a measurement of the neat D_2O subphase salt solution is included in Figure 2, with a fit to the data (dashed line) corresponding to a roughness of 2.8 Å, in good agreement with what is expected from capillary wave theory (15). Neutron reflectivity was measured at two angles of incidence for a monolayer of 19-MEA and EA, both at zero surface pressure and at the highest measured surface pressure for each system. For all other surface pressures, the monolayer was measured only at the higher angle of incidence since these data contained the primary region of interest ($q_z \geq 0.05$ Å^{-1})

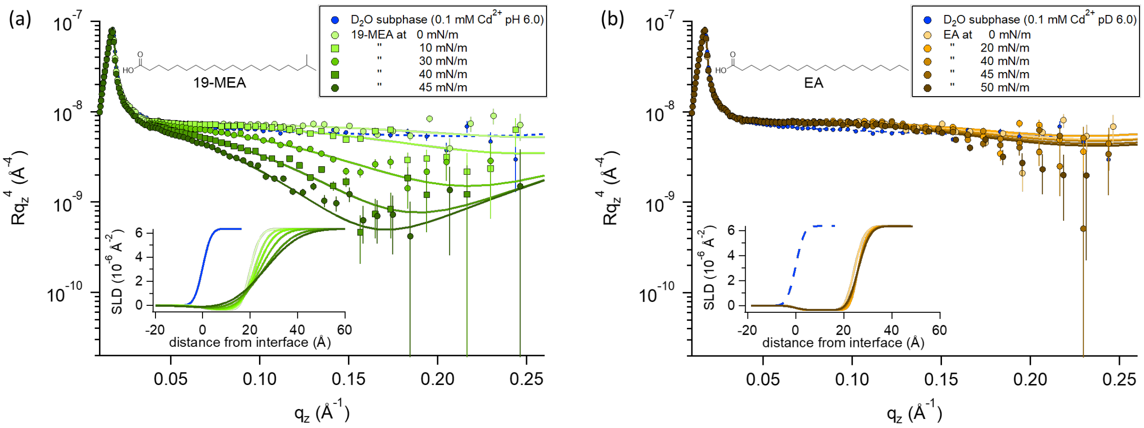

Figure 2. *Neutron reflectivity of 19-MEA (a) and EA (b) at different surface pressures on a D_2O subphase with 0.1 mM $CdCl_2$ buffered to pD 6.0. The reflectivity is shown as a multiple of q_z^4 to emphasise intensity variations at increasing q_z-values. Markers are showing experimental data. Squares and circles are used to differentiate the data sets. Corresponding model fits are represented with solid lines. The insets show SLD-profiles of the data fits using a two-layer model dividing the headgroup and the aliphatic tail.*

All experiments were carried out with hydrogenous fatty acids on a pH buffered D_2O salt solution subphase, which is only one of the possible isotopic contrast combinations of the surfactant and subphase. This provides the optimal contrast to specifically probe the flatness of the planar water interface itself, rather than structural aspects of the monolayer. (The scattering length density of hydrocarbon is close to that of air, which renders it effectively invisible to neutrons). For NR, this lack of contrast is normally seen as a drawback because of the lack of sensitivity to chain length determination. However, thanks to this weak scattering of the aliphatic tails, the reflectivity signal is *dominated* by the texturing of the D_2O surface.

According to capillary wave theory, an increase in surface pressure of a fluid monolayer at the water–air interface should lead to an increased capillary wave amplitude. This is not observed in the reflectivity of EA, however, where the roughness in fact first decreases, before then increasing only slightly over the applied surface pressure range. Such behaviour has been observed earlier, and was explained by the increasing monolayer rigidity suppressing the capillary wave roughness for the straight chain fatty acid behenic acid (43). Analogously, this should explain the observed behaviour for EA since it enters the untilted condensed phase directly upon lift-off (44) of the pressure–area isotherm (shown in Figure S1 in SI—where this is further discussed together with Figure S4). Lateral fluctuations in the scattering length density of the interface due to domain formation on the scale shown in Figure 1, would be far below the neutron coherence length, which is on the micrometre scale in these experiments. The implication is that the measured neutron reflectivity is determined from the scattering length density (SLD) depth profile that is averaged across the whole sample. This in turn allows fitting of the data using a slab model based on the reflection of neutrons at stratified media (20, 21) where a roughness term can be used to account for any inhomogeneity across the surface as well as the roughness due to capillary waves.

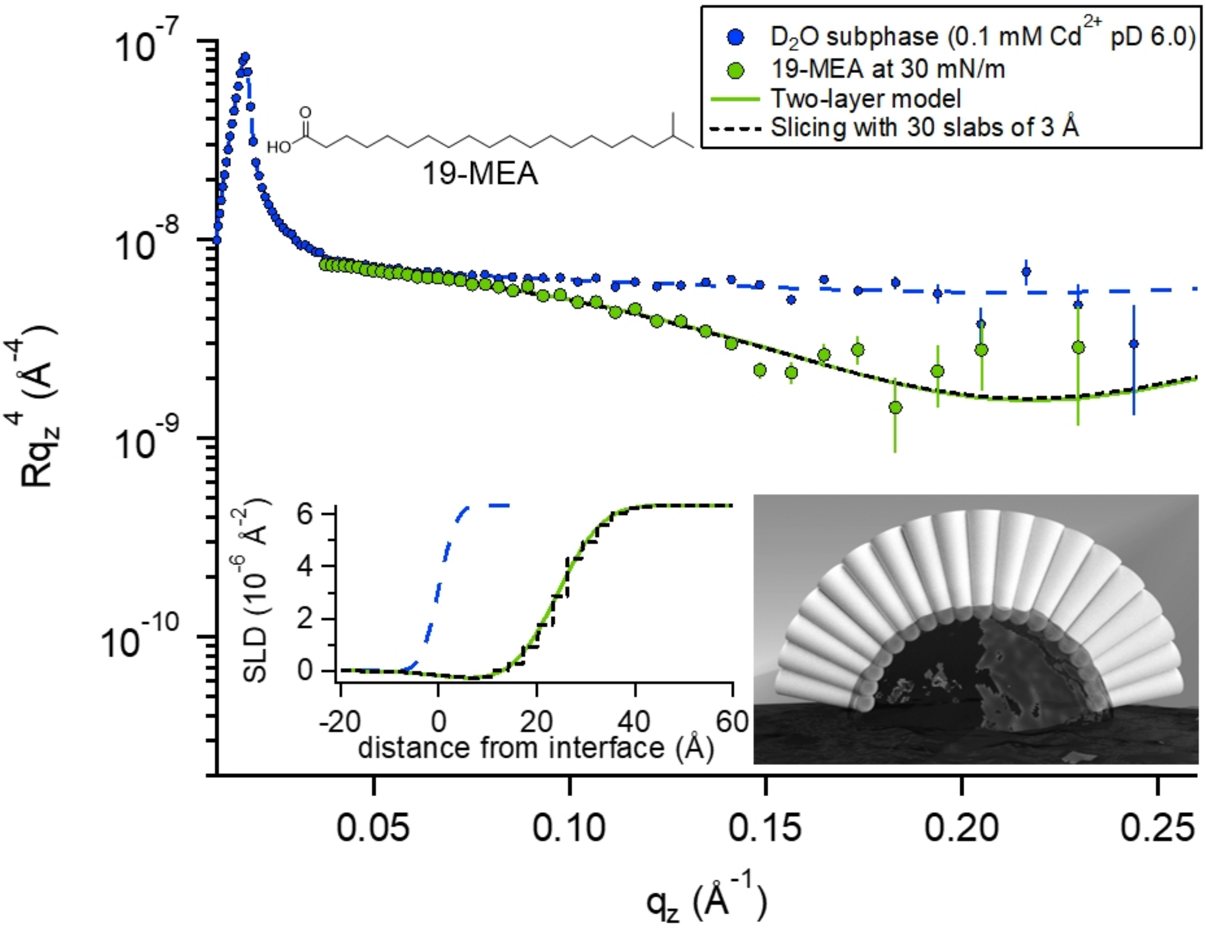

Figure 3. *Neutron reflectivity of 19-MEA at 30 mN m^{-1} on a D_2O subphase with 0.1 mM $CdCl_2$ and buffered to pD 6.0. Measurement of a neat D_2O solution subphase is shown with small circles with the dashed blue line representing a fit to capillary wave of 2.8 Å. The solid line and the dotted lines represent fits to the data using a two-layer model with relatively high but identical interfacial roughness, and a 30-slab model with no interfacial roughness, respectively. Each slab is 3 Å thick. The insets show the SLD-profiles and a schematic representation of the hypothesised texturing of the water–air interface due to tail group packing constraints.*

A two-layer model was required to fit the data, separating the distinctly different scattering properties of the fatty acid headgroups and the aliphatic tails. Fitting parameters and a detailed explanation of the fitting procedures for 19-MEA and EA are presented in the SI. Note that conventional 2D monolayer fitting approaches need to be adapted somewhat to model a textured surface, the details of which are given in the Methods section. Attempts to fit the system with a one-layer model of smeared SLD did not give satisfactory correlation with the data. Moreover, it has recently been shown that the use of a one-layer model to fit neutron reflectivity data from surfactant monolayers in a limited number of isotopic contrasts can result in erroneous interpretations, particularly when unsupported by data from other isotopic contrasts, and this problem is avoided through use of a two-layer model (45). Such a two-layer model with low roughness (corresponding to the amplitude of capillary waves) provides an excellent fit to the EA data (see table 1 in SI) since it is known that the monolayer forms a homogeneous 2D monolayer. To fit the 19-MEA data, however, it was necessary to invoke a significantly higher surface roughness, consistent with the idea of a 3D textured water interface. For a system modelled with layers of varying scattering length density, the introduction of a roughness parameter is used to describe interfacial mixing of the two layers as a Gaussian error function. In a system of stratified media with an interfacial roughness on the order of the layer thickness itself, the error functions between layers can overlap, leading to unphysical calculated densities in the interfacial region. It has been shown that this problem is avoided, however, by choosing identical roughness values at all interfaces (45). To verify that not only is the SLD calculation physically reasonable, but also that the reflectivity calculations used to fit the data (based on roughness-modified stratified media with Fresnel reflectivity) are valid, one dataset was fitted in two different ways. The premise for this verification is described in more depth in the Neutron Reflectivity Fitting section. Approach 1 is a conventional fit using a two-layer model (as for EA) but employing higher, identical, interfacial roughness at each interface. Approach 2 involves the generation of a SLD profile using almost the same physical density distribution of the material at the interface, but which is instead sliced into 30 layers of 3 Å thickness with zero interfacial roughness to eliminate the possibility of artefacts in the data from the relatively high roughness. Figure 3 shows an example of these two data fitting approaches for the case of 19-MEA on the D_2O subphase at a surface pressure of 30 m Nm^{-1}. For the two-layer model, the (identically constrained) interfacial roughness was fitted as 7.0 Å, with headgroup and tail region thicknesses of 4.5 Å and 23.5 Å, respectively. The solid line represents the two-layer model fit and the dashed black line represents the slicing fit with zero roughness. The insets show the resulting SLD-profiles as well as a schematic representation of the suggested hypothesis for self-assembly-induced texturing of the water–air interface. The fits overlap to the point of being almost indistinguishable. This demonstrates that the Fresnel reflectivity calculation with the added Gaussian error function is valid and equivalent to the standard Fresnel calculation of stratified media, even when the topographic variation far exceeds the layer thickness. This empirical validation of the use of identically constrained high roughness values, should be generally applicable to multiple stratified systems, for example phospholipid monolayers where both head and tail are deuterated (45).

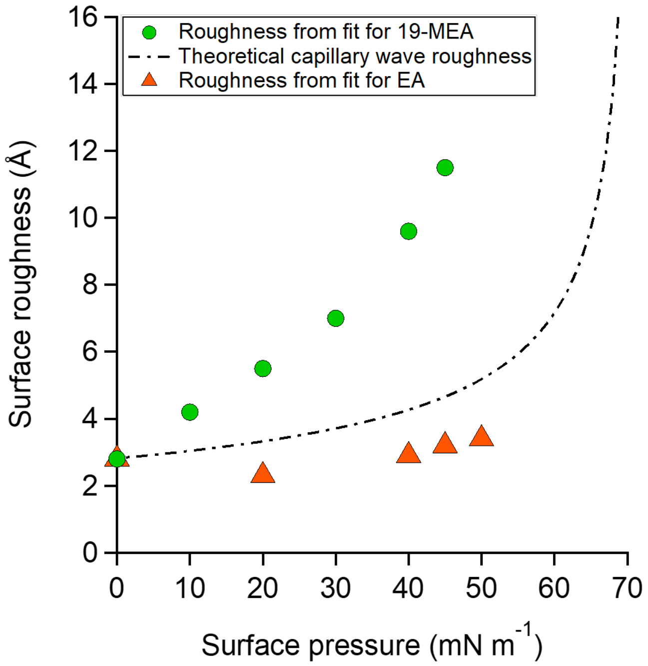

Figure 4 *Variation of the surface roughness used to fit experimental NR data for 19-MEA (green circles) and EA (orange triangles) shown together with the theoretically expected increase in surface roughness due to thermally excited capillary waves of water (dashed line) with decreasing surface tension on the assumption that the monolayer is fluid and disordered.*

The fitting parameters for 19-MEA, extracted from the two-layer slab model, are shown in Table 2 of the SI. The large range of surface pressures measured were accessed through rather minor changes of surface area (and resulting area per molecule), due to the steepness of the surface pressure–area isotherm, and thus it would not be expected that there should be significant changes in any of the density or thickness parameters corresponding to the fatty acid. Therefore, the only fitting parameter was the roughness of all the interfaces in the slab model, which were constrained to be equal to each other. For 19-MEA, the hydrocarbon region thickness was also varied slightly and systematically based on the isotherm data. The SLD values of the hydrocarbon and headgroup region were calculated, and the headgroup region thickness was constrained to the same calculated value for both EA and 19-MEA. The only parameter capable of inducing the observed decrease in intensity in Figure 2 is the interfacial roughness parameter (constrained to be identical at each of the three interfaces in the two-layer model). The roughness parameters for the model fits to the experimental data for EA and 19-MEA are presented in Figure 4 with respect to the surface pressure, together with a theoretical prediction of capillary wave roughness based on the assumption of a fluid monolayer (15, 46). As noted earlier, the data from EA demonstrates that its surface roughness is less than the model predicts, which is attributed to the bending rigidity of the molecule. Importantly, the increased roughness of the water–air interface observed for 19-MEA far exceeds that which can be argued to originate exclusively from the presence of capillary waves, even ignoring the damping effect. Therefore, these results together provide the first direct *in situ* evidence for 3D texturing of the water–air interface using a simple surfactant monolayer.

The schematic inset in Figure 3 shows a possible spherical cap structuring of the 19-MEA films, consistent with both the NR fits and the AFM images. The cartoon underestimates the number of molecules in the domains, which would be of the order of 9000, with a much larger radius of curvature. The calculation of the number of molecules per surface domain is shown in the SI.

The AFM images reveal that the aggregates, which exist already at 0 mN m^{-1} are further organised into monodisperse domains of hexagonal ordering at 40 mN m^{-1}. There is no observable coalescence between domains. Their monodispersity suggests an optimal size corresponding to an energy minimum, analogous to the monodispersity of other surfactant self-assembly structures such as micelles and microemulsions, where the aggregate curvature is determined by the so-called packing parameter (47, 48). To extend this self-assembly analogy, to the water–air interface, this optimal size would then correspond to a spherical cap with a radius of curvature governed by the fatty acid tail group packing. The presence of the methyl group prevents the close parallel packing of the alkyl chains, which leads to a flat monolayer in the case of the unbranched molecules, and imposes a negative curvature for the branched molecules. The larger topography (measured as increased surface roughness) at higher surface pressure implies that closer packing of the monolayer yields a larger perturbation—or lifting—of the water surface. Thus, it can be concluded that self-assembly of surface domains alone does not perturb the water surface, but that compression of the domain-containing monolayer is also necessary if three-dimensional texturing is to be achieved, and the rule of a flat planar water interface under gravity is to be broken.

So far, AFM measurements indicate the lateral size of the domains (but no height information since the monolayers are deposited on a rigid solid interface) and the NR studies indicate a measure of their height (or texturing) but with no explicit information on their lateral extent. While compelling, these independent observations do not completely prove the hypothesis of self-assembly based curvature. If the suggested mechanism is correct, however, it should then be possible to use equations describing the geometry of a spherical cap to predict the radius of curvature from the normal and lateral dimensions, respectively, provided by the two completely independent techniques. Such a calculation is performed in the SI. Using the diameter of 50 nm for the 45 mM m^{-1} case, and assuming that the Gaussian roughness in fact is an estimation of the average height of the spherical caps, h = 11.5 Å at the same pressure, a curvature radius of 2.5 μm is obtained. In reference (36) a simple estimation of the curvature is proposed based on molecular areas. Using the areas per molecule at 45 mN m^{-1} from that paper, a radius of curvature is calculated with no free parameters, corresponding to 2.7 μm. These values differ by only 8% which is extraordinarily good agreement given the simplicity of the calculations in each case and provides categorical support for the self-assembly model.

The notion of a planar water interface under gravity has been challenged. In the present work, it has been directly shown that the biomimetic, methyl-branched long chain fatty acid 19-MEA perturbs the flatness of the water–air interface by several Ångströms to create 3D surface domains with a height modulation that far exceeds that expected for capillary waves. The straight chain analogue EA on the other hand does not exhibit this behaviour and in fact displays a lower surface roughness than capillary wave theory predicts for a fluid, disordered monolayer, which is explained by its high bending rigidity. The novel 3D surface texturing for the 19-MEA system is attributed to packing constraints in its branched, saturated chains. This advance thus provides the opportunity to template the liquid–air interface itself with nanosized, regularly ordered asperities through control of the surfactant packing parameter; via chain branching, chain substitution, unsaturation or multiple chains, which was not apparent before. Controlled nano-structuring of sol-gel polymerisation at the water–monolayer interface, or UV-initiated monolayer polymerisation, are two potential pathways of exploitation, utilising either side of the textured surface. Further, while the applications of deposited Langmuir-Blodgett films generally require homogeneous monolayers, there is a clear opportunity to tune the architecture of such films. Regular patterns can be generated, of nm thickness, nanoscale-microscale lateral dimensions with uniform size over areas which could be on the scale of square metres! These 3D species could then be used to decorate a solid surface with regular patterns on the nm scale, transformed to 2D due to the rigidity of the solid. As is known from

100 years or so of research into microemulsions and micellar aggregates, self-assembly is exquisitely tuneable in terms of curvature and thus lateral dimensions. Both the polar headgroup area and the non-polar region can be independently tuned in size and anisotropy and these tools already exist. Since metal ions are associated with the fatty acids (in this case) it should be feasible to deposit nm size islands consisting of a few hundred metal ions in each which could then be reduced to form metallic nanodots, avoiding costly printing and nanotechnology solutions, which are usually feasible only over smaller areas. Unlike many soft nanomaterial breakthroughs, requiring sophisticated equipment, printers, advanced lithography and so on, these large-scale patterns on nm scale could be generated by undergraduates in the laboratory on the first attempt, using chemicals they buy from a catalogue.

A planar water interface under gravity is thus not necessarily a self-levelling two-dimensional environment, supporting self-assembly structures and moderated only by the presence of capillary waves, as previously believed, but can support a significant degree of static topography.

ACKNOWLEDGEMENTS

We thank the ILL for the provision of neutron beam time on FIGARO (DOI: 10.5291/ILL-DATA.9-10-1487). MR and EB acknowledge support from the Swedish Research Council via grant VR 2013-04384. PMB acknowledges funding from the Excellence Cluster Nanosystems Initiative Munich (NIM) and the Center for NanoScience (CeNS). We thank Gustavo Luengo, Deborah Wakeham, Anna Oleshkevych, Philipp Gutfreund, and Adrian Rennie for useful discussions.

COMPETING INTERESTS

The authors declare no competing interests.

MATERIALS AND METHODS

All chemicals were used as received. The fatty acids were provided by Sigma Aldrich (EA ≥99%, 19-MEA >98%). Chloroform (Sigma Aldrich, ≥99.5%, stabilised with 100-200 ppm amylene) was used to spread fatty acid monolayers on a water and D_2O subphase for Langmuir-Blodgett depositions and NR measurements, respectively. In both cases, the subphase contained 0.1 mM $CdCl_2$, 0.1 mM $NaHCO_3$, and was buffered to pH (or pD) 6.0 with HCl (or DCl) to stabilise and condense the monolayer (7, 9). A KSV NIMA 5000 PTFE (polytetrafluoroethylene) trough with hydrophilic POM (polyoxymethylene) barriers was used for depositions. For NR measurements a similar, but smaller trough was used, which was stabilised on-line by an active anti-vibration table. Barriers were symmetrically compressed at 4.5 cm^2 min^{-1}. Wilhelmy plates of paper were used to monitor surface pressure and the subphase was temperature controlled to 22 °C. Monolayers were deposited at 1 mm min^{-1} onto silicon wafers, cleaned by immersion in chromosulfuric acid (5% Cr(VI) in H_2SO_4) and thoroughly rinsed with MilliQ water. AFM imaging of deposited monolayers was done with a Bruker Multimode Microscope LN in tapping mode, using silicon cantilevers (HQ:NSC35/AL BS, MikroMasch) with a typical radius of 8 nm. The nominal resonance frequency and force constant of the cantilevers were 150 kHz and 5.4 N m^{-1}, respectively. Analysis of representative 1 μm by 1 μm AFM images was performed in WSxM 5.0 (49). NR measurements were performed at the horizontal time-of-flight reflectometer FIGARO at Institut Laue-Langevin (ILL) in Grenoble, France (50). Reflectivity was acquired at two angles of incidence, $\theta = 0.62°$ and $\theta = 3.8°$ with a wavelength resolution of 7 % $d\lambda/\lambda$, and 2D detector at 2890 mm from the sample stage, situated in an evacuated flight tube. The intensity of specular reflected neutrons was normalized to the incident neutron beam as a function of angle and neutron wavelength according to the momentum transfer q_z along the surface normal

$$q_z = \frac{4\pi}{\lambda}\sin(\theta) \qquad (1)$$

where λ is the neutron wavelength and θ is the angle of incidence. All NR measurements were made with hydrogenous surfactants on D_2O salt solutions. The reflectivity profiles were analysed using Motofit (51).

Neutron Reflectivity Fitting

The application of a slab, or layer, model where the topographic variation or roughness is large compared to the layer thickness is not without controversy (45, 52–54). Reference 44 demonstrated conservation of material in the SLD-profile through application of relatively high but identical roughness values at the three interfaces present in the two-layer model of a surfactant monolayer at the water–air interface (water–headgroups, headgroups–tails, and tails–air). This conservation of material may not be maintained if different roughness values that are significantly large with respect to the smallest layer thickness are applied at the respective interfaces because an artefact in the form of a region of negative density can appear in the density profiles normal to the interface. Therefore, it was concluded that application of roughness values as large as the smallest layer thickness is a physically reasonable approach. The work, however, stopped short of demonstrating that the application of such relatively high, but identical roughness values results in physically realistic reflectivity calculations. This point is now addressed by examining whether the reflectivity calculations are correctly described by a model where the "roughness" (the factor accounting for the smearing of the SLD in the vertical direction by the topography variation) is as large as—or ever larger than—the smallest layer thickness. The Fresnel coefficients in Equation (2) are used to describe reflection and refraction in stratified media. Due to interdiffusion or surface perturbations, or both, a Gaussian error function is added to account for the deviation from homogeneous slab behaviour (55)

$$r_{i,i+1} = \frac{k_i - k_{i+1}}{k_i + k_{i+1}} \exp\left(-2k_i k_{i+1} \sigma_{i,i+1}^2\right) \tag{2}$$

where k denotes the wave vector and σ the interfacial roughness term for each of i layers. For systems of high roughness, the error functions of separate layers can overlap, which for unconstrained roughness values may invalidate the physical validity of the model. If the roughnesses are constrained to be identical, then this potential problem may be avoided. As a test, it was shown in the present work that a fit to the reflectivity data is possible, using Fresnel reflectivities generated by a so-called slicing model. In this case the SLD profile is generated by dividing the interface into 30 layers of 3 Å thickness with zero interfacial roughness but maintaining the same physical density distribution as generated by the 2-layer model. (This workflow is shown in the SI). The SLD profile is calculated by

$$\rho_z \sum_{n=1}^{N} \frac{\rho_n - \rho_{n+1}}{2} \left(1 + \operatorname{erf} \left(\frac{z - z_n}{\sqrt{2}\sigma_n} \right) \right) \tag{3}$$

where N is the total number of layers, z is the distance from the top interface, σ is the interfacial roughness, and "erf" is the error function (51).

REFERENCES

1. Kaganer V, Möhwald H, Dutta P (1999) Structure and phase transitions in Langmuir monolayers. *Rev Mod Phys* 71(3):779–819.
2. Brezesinski G, Möhwald H (2003) Langmuir monolayers to study interactions at model membrane surfaces. *Adv Colloid Interface Sci* 100–102:563–584.
3. King MD, et al. (2009) Oxidation of oleic acid at the air-water interface and its potential effects on cloud critical supersaturations. *Phys Chem Chem Phys* 11(35):7699–7707.
4. Pezron E, Claesson PM, Berg JM, Vollhardt D (1990) Stability of arachidic acid monolayers on aqueous salt solutions. *J Colloid Interface Sci* 138(1):245–254.
5. Eng LM, Seuret C, Looser H, Gunter P (1996) Approaching the liquid/air interface with scanning force microscopy. *J Vac Sci Technol B Microelectron Process Phenom* 14(2):1386.
6. Kjaer K, et al. (1991) X-Ray Scattering Studies of Organic Monolayers on Electrolytic Solutions: Arachidic Acid on CdCl2. *Proceedings of the 2nd International Conference, Physik Zentrum, Bad Honnef, Fed. Rep. of Germany*, pp 143–146.
7. Binks BP (1991) Insoluble monolayers of weakly ionising low molar mass materials and their deposition to form Langmuir-Blodgett multilayers. *Adv Colloid Interface Sci* 34(C):343–432.
8. Kundu S, Datta A, Hazra S (2005) Effect of metal ions on monolayer collapses. *Langmuir* 21(13):5894–5900.
9. Kmetko J (2002) Effects Of Divalent Ions On Langmuir Monolayers : Synchrotron X-ray Scattering Studies.
10. Peng JB, Barnes GT, Gentle IR (2001) The structures of Langmuir-Blodgett films of fatty acids and their salts. *Adv Colloid Interface Sci* 91(2):163–219.

11. Pockels A, (Rayleigh) (1891) Surface Tension. *Nature* 43(1115):437–439.

12. Gaines GL (1966) *Insoluble Monolayers at Liquid-gas Interfaces* (Interscience Publishers).

13. Barnes G, Gentle I (2011) *Interfacial science : an introduction* (Oxford University Press).

14. Matijević E (1979) Principles of colloid and surface chemistry. *J Colloid Interface Sci* 70(2):399.

15. Braslau A, Pershan PS, Swislow G, Ocko BM, Als-Nielsen J (1988) Capillary waves on the surface of simple liquids measured by x-ray reflectivity. *Phys Rev A* 38(5):2457–2470.

16. Sinha SK, Sirota EB, Garoff S (1988) X-ray and neutron scattering from rough surfaces. *Phys Rev B* 38(4):2297–2311.

17. Petrov JG, Pfohl T, Möhwald H (1999) Ellipsometric Chain Length Dependence of Fatty Acid Langmuir Monolayers. A Heads-and-Tails Model. *J Phys Chem B* 103(17):3417–3424.

18. Bohanon TM, Lin B, Shih MC, Ice GE, Dutta P (1990) Determination of lattice structure and calculation of molecular tilt in lipid monolayers on water using x-ray diffraction. *Phys Rev B Condens Matter* 41(7):4846–4849.

19. Peng JB, Barnes GT, Gentle IR, Foran GJ (2000) Superstructures and Correlated Metal Ion Layers in Langmuir−Blodgett Films of Cadmium Soaps Observed with Grazing Incidence X-ray Diffraction. *J Phys Chem B* 104(23):5553–5556.

20. Bradley J, Lee E, Thomas R, Penfold J, Ward R (1988) Adsorption at the Liquid Surface Studied by Means of Specular Reflection of Neutrons. *Langmuir* 80(4):821–826.

21. Pfrang C, et al. (2014) Ozonolysis of methyl oleate monolayers at the air–water

interface: oxidation kinetics, reaction products and atmospheric implications. *Phys Chem Chem Phys* 16(26):13220–13228.

22. Tyrode E, Rutland MW, Bain CD (2008) Adsorption of CTAB on hydrophilic silica studied by linear and nonlinear optical spectroscopy. *J Am Chem Soc* 130(51):17434–17445.
23. Ma G, Allen HC (2006) DPPC Langmuir monolayer at the air-water interface: Probing the tail and head groups by vibrational sum frequency generation spectroscopy. *Langmuir* 22(12):5341–5349.
24. Schwartz DK, Viswanathan R, Garnaes J, Zasadzinski JA (1993) Influence of Cations, Alkane Chain Length, and Substrate on Molecular Order of Langmuir-Blodgett Films. *J Am Chem Soc* 115(18):7374–7380.
25. Peng JB, Barnes GT (1994) The two-dimensional hexatic-B phase of single Langmuir-Blodgett monolayers observed by atomic force microscopy. *Thin Solid Films* 252(1):44–48.
26. Kato T, Kameyama M, Ehara M, Iimura K-I (1998) Monodisperse Two-Dimensional Nanometer Size Clusters of Partially Fluorinated Long-Chain Acids. *Langmuir* 7463(15):1786–1798.
27. Krafft MP (2012) Large organized surface domains self-assembled from nonpolar amphiphiles. *Acc Chem Res* 45(4):514–524.
28. De Viguerie L, et al. (2011) Effect of the molecular structure on the hierarchical self-assembly of semifluorinated alkanes at the air/water interface. *Langmuir* 27(14):8776–8786.
29. Malone SM, Trabelsi S, Zhang S, Lee TR, Schwartz DK (2010) Self-assembly of linactants: Micelles and lyotropic liquid crystals in two dimensions. *J Phys Chem B* 114(26):8616–8620.

30. Fontaine P, et al. (2005) Direct evidence for highly organized networks of circular surface micelles of surfactant at the air-water interface. *J Am Chem Soc* 127(2):512–513.

31. Silva GMC, Morgado P, Lourenço P, Goldmann M, Filipe EJM (2019) Spontaneous self-assembly and structure of perfluoroalkylalkane surfactant hemimicelles by molecular dynamics simulations. *Proc Natl Acad Sci* 116(30):14868–14873.

32. Micciulla S, Gerelli Y, Campbell RA, Schneck E (2018) A Versatile Method for the Distance-Dependent Structural Characterization of Interacting Soft Interfaces by Neutron Reflectometry. *Langmuir* 34(3):789–800.

33. Reguera J, et al. (2015) Contact angle and adsorption energies of nanoparticles at the air-liquid interface determined by neutron reflectivity and molecular dynamics. *Nanoscale* 7(13):5665–5673.

34. Lu JR, Su TJ, Thomas RK, Penfold J, Webster J (1998) Structural conformation of lysozyme layers at the air/water interface studied by neutron reflection. *J Chem Soc - Faraday Trans* 94(21):3279–3287.

35. Atkinson PJ, Dickinson E, Horne DS, Richardson RM (1995) Neutron reflectivity of adsorbed β-casein and β-lactoglobulin at the air/water interface. *J Chem Soc Faraday Trans* 91(17):2847–2854.

36. Liljeblad JFD, et al. (2014) Self-assembly of long chain fatty acids: effect of a methyl branch. *Phys Chem Chem Phys* 16(33):17869–17882.

37. Wertz PW, Downing DT (1988) Integral lipids of human hair. *Lipids* 23(9):878–881.

38. Jones LN, Rivett DE (1997) The role of 18-methyleicosanoic acid in the structure and formation of mammalian hair fibres. *Micron* 28(6):469–485.

39. Negri A, Cornell H, Rivett D (2004) The nature of Covalently bound fatty acids in wool fibres. *Aust J Agric Res* 42(8):1285.

40. Tanford C (1972) Micelle shape and size. *J Phys Chem* 76(21):3020–3024.

41. Birdi KS, Vu DT (1994) Structures of lipid and biopolymer monolayers investigated as Langmuir-Blodgett films by atomic force microscopy. *Surf Coatings Technol* 67(3):183–191.

42. Das K, Kundu S (2016) Subphase pH induced monolayer to multilayer collapse of fatty acid Salt Langmuir monolayer at lower surface pressure. *Colloids Surfaces A Physicochem Eng Asp* 492:54–61.

43. Daillant J, Bosio L, Benattar JJ, Meunier J (1989) Capillary Waves and Bending Elasticity of Monolayers on Water Studied by X-Ray Reflectivity as a Function of Surface Pressure. *Eur Lett* 8(1):453–458.

44. Kurnaz ML, Schwartz DK (1996) Morphology of Microphase Separation in Arachidic Acid/Cadmium Arachidate Langmuir-Blodgett Multilayers. *J Phys Chem* 100(26):11113–11119.

45. Campbell RA, et al. (2018) Structure of surfactant and phospholipid monolayers at the air/water interface modeled from neutron reflectivity data. *J Colloid Interface Sci* 531:98–108.

46. Braslau A, et al. (1985) Surface roughness of water measured by x-ray reflectivity. *Phys Rev Lett* 54(2):114–117.

47. Israelachvili JN, Mitchell DJ, Ninham BW (1976) Theory of self-assembly of hydrocarbon amphiphiles into micelles and bilayers. *J Chem Soc Faraday Trans 2 Mol Chem Phys* 72(0):1525–1568.

48. Nagarajan R (2002) Molecular packing parameter and surfactant self-assembly: The neglected role of the surfactant tail. *Langmuir* 18(1):31–38.

49. Horcas I, et al. (2007) WSXM: A software for scanning probe microscopy and a tool for nanotechnology. *Rev Sci Instrum* 78(1):013705.

50. Campbell RA, Wacklin HP, Sutton I, Cubitt R, Fragneto G (2011) FIGARO: The new horizontal neutron reflectometer at the ILL. *Eur Phys J Plus* 126(11):107.

51. Nelson A (2006) Co-refinement of multiple-contrast neutron/X-ray reflectivity data using MOTOFIT. *J Appl Crystallogr* 39(2):273–276.

52. Vidal B, Vincent P (2009) Metallic multilayers for x rays using classical thin-film theory. *Appl Opt* 23(11):1794.

53. De Boer DKG (1994) Influence of the roughness profile on the specular reflectivity of x rays and neutrons. *Phys Rev B* 49(9):5817–5820.

54. Jia D, et al. (2011) Dynamic adsorption and structure of interfacial bilayers adsorbed from lipopeptide surfactants at the hydrophilic silicon/water interface: Effect of the headgroup length. *Langmuir* 27(14):8798–8809.

55. Névot L, Croce P (1980) Caractérisation des surfaces par réflexion rasante de rayons X. Application à l’étude du polissage de quelques verres silicates. *Rev Phys Appliquée* 15(3):761–779.

Supplementary Information

3D texturing of the water–air interface by biomimetic self-assembly.

Erik Bergendal,[1] Richard A. Campbell,[2,3] Georgia A. Pilkington,[1] Peter Müller-Buschbaum,[4,5] Mark W. Rutland,*[1,6]

---

[1] Surface and Corrosion Science, School of Engineering Sciences in Chemistry, Biotechnology and Health, KTH Royal Institute of Technology, Drottning Kristinas väg 51, 100 44 Stockholm Sweden

[2] Institut Laue-Langevin, 71 avenue des Martyrs, 38042 Grenoble, France

[3] Division of Pharmacy and Optometry, University of Manchester, Manchester M21 9PT, UK.

[4] Physik-Department, Lehrstuhl für Funktionelle Materialen, Technische Universität München, James-Franck-Str.1, 85748 Garching, Germany

[5] Heinz Maier-Leibnitz Zentrum (MLZ), Technische Universität München, Lichtenbergstr. 1, 85748 Garching, Germany

[6] RISE Research Institutes of Sweden, Chemistry, Materials and Surfaces, Box 5607, SE-114 86 Stockholm, Sweden

Supplementary data

S1 Surface pressure–area isotherms of EA and 19-MEA

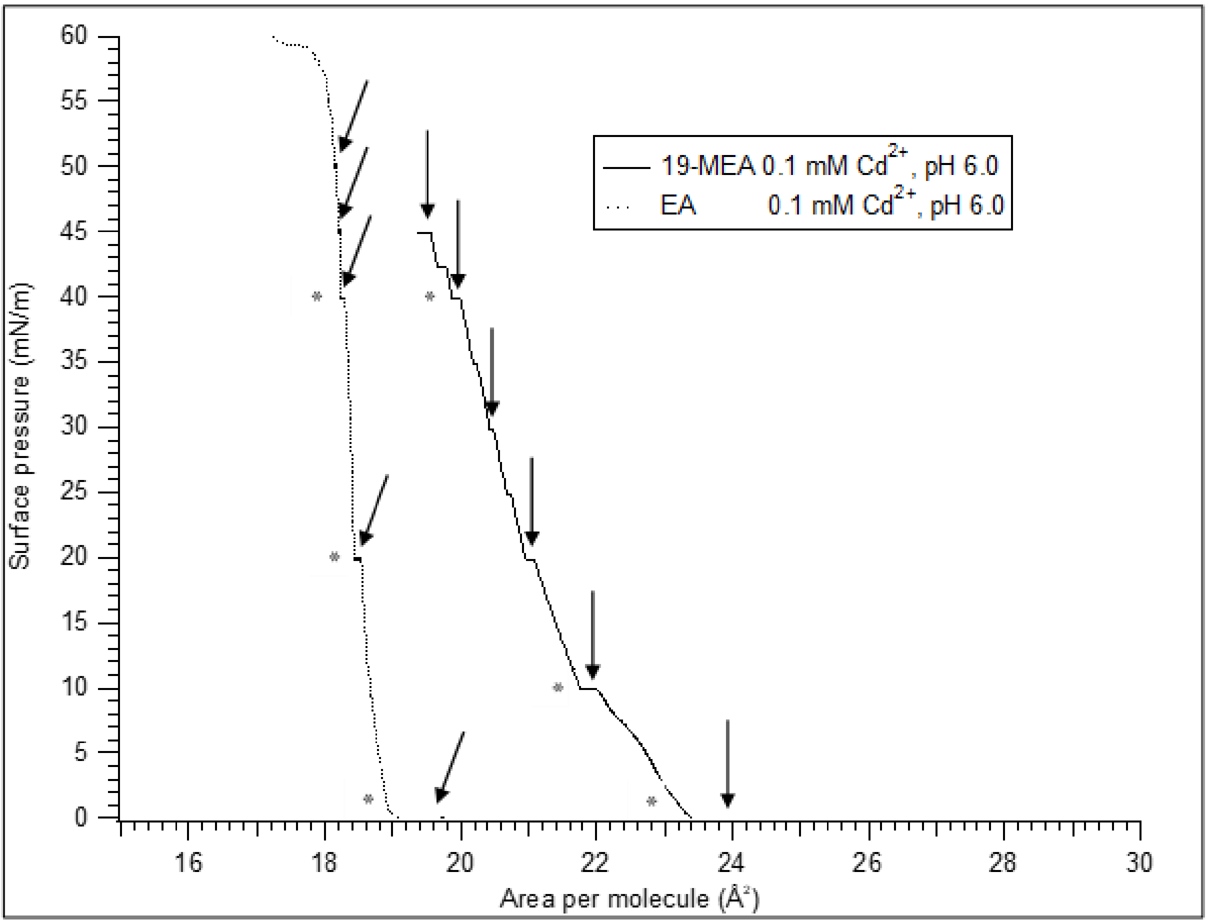

S1 Pressure–Area isotherm of EA and 19-MEA collected during NR experiment. The isotherms have been shifted in area per molecule for comparison with Liljeblad et al. (56). Stars and arrows show pressure at deposition and NR measurement, respectively. The decreased area per molecule during experiment is the result of continuous monolayer collapse when the surface pressure is held constant above its equilibrium spreading pressure (57).

S2 AFM characterisation of unbranched fatty acid monolayer

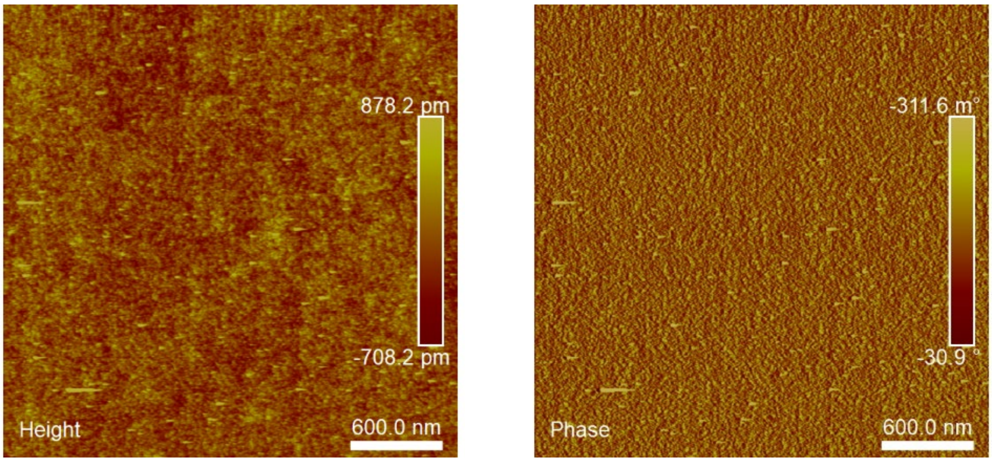

*S2 AFM height and phase image of deposited EA monolayer at 40 mN m^{-1}, showing a featureless morphology. Nanometer-sized multilayer patches are visible in the height image corresponding to trilayering seen in continuous monolayer collapse when held at constant pressure. In accordance with theory by Vollhardt (58)***.***

S3 AFM characterisation of unbranched fatty acid monolayer with height profile

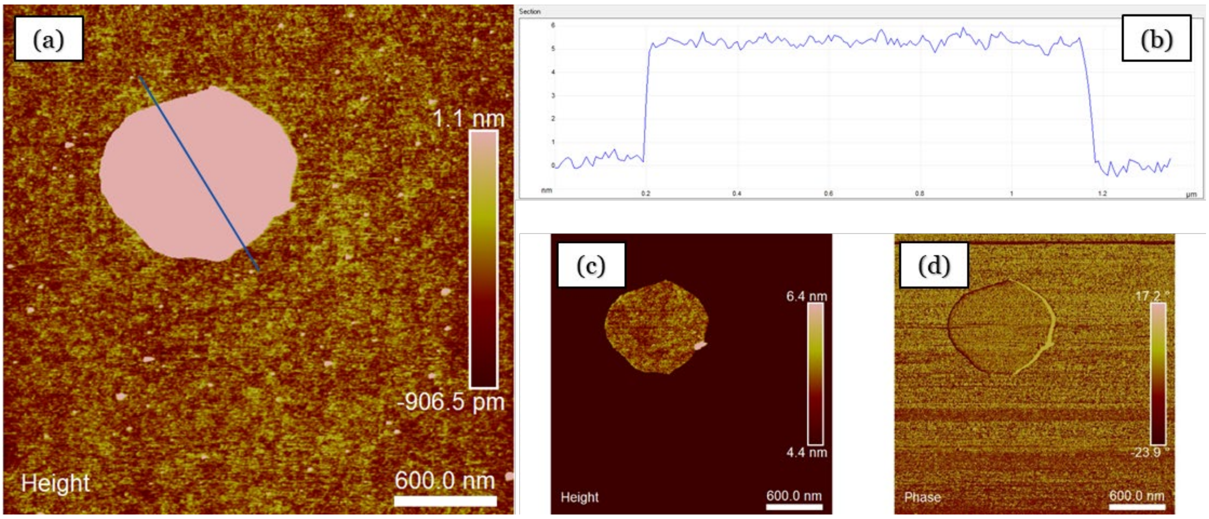

S3. (a) *AFM height image of deposited monolayer of EA at 20 mN m^{-1} showing a flat monolayer with a multilayer patch. With an extended chain length of ~25 Å this corresponds well to an expected trilayer as shown by the line profile in (b), which was taken over the particle. Image (c) shows the same image as (a) with a shifted height scale to emphasise the agreement in height profile of the monolayer and trilayer. Finally, (d) shows the phase image which confirms the same mechanical properties of the monolayer and the trilayer patch.*

Neutron fitting parameters

Tables below shows fitting parameters used to generate fits for EA and 19-MEA as ST 1 and ST 2, respectively.

ST 1. *Parameters used to fit NR data of EA using a two-layer model.*

Model parameter	0 mN m^{-1}	20 mN m^{-1}	40 mN m^{-1}	45 mN m^{-1}	50 mN m^{-1}	free D2O surface
thickness tail (Å)	23.9	25.5	25.5	25.5	25.5	
thickness headgroup (Å)	4.5	4.5	4.5	4.5	4.5	
SLD tail (x10^{-6} Å^{2})	-0.36	-0.36	-0.36	-0.36	-0.36	
SLD headgroup (x10^{-6} Å^{2})	4.7	4.7	4.7	4.7	4.7	
SLD backing (x10^{-6} Å^{2})	6.357	6.357	6.357	6.357	6.357	6.357
solvent penetration %	33	33	33	33	33	
roughness tail (Å)	2.8	2.3	2.9	3.2	3.4	
roughness headgroup (Å)	2.8	2.3	2.9	3.2	3.4	
roughness backing (Å)	2.8	2.3	2.9	3.2	3.4	2.83
BACKGROUND						
3.8E-7						
SCALE						
1						

ST 2. *Parameters used to fit NR data of 19-MEA using a two-layer model.*

Model parameter	0 mN m^{-1}	10 mN m^{-1}	20 mN m^{-1}	30 mN m^{-1}	40 mN m^{-1}	45 mN m^{-1}	free D_2O surface
thickness tail (Å)	19.5	21	22.5	23.5	25	25.5	
thickness headgroup (Å)	4.5	4.5	4.5	4.5	4.5	4.5	
SLD tail (x10^{-6} Å^{2})	-0.36	-0.36	-0.36	-0.36	-0.36	-0.36	
SLD headgroup (x10^{-6} Å^{2})	4.7	4.7	4.7	4.7	4.7	4.7	
SLD backing (x10^{-6} Å^{2})	6.357	6.357	6.357	6.357	6.357	6.357	6.357
solvent penetration %	33	33	33	33	33	33	
roughness tail (Å)	2.8	4.2	5.5	7.0	9.6	11.5	
roughness headgroup (Å)	2.8	4.2	5.5	7.0	9.6	11.5	
roughness backing (Å)	2.8	4.2	5.5	7.0	9.6	11.5	2.83
BACKGROUND							
3.8E-7							
SCALE							
1							

Supplementary methods

Fitting procedures: two-layer and slicing model

In the fitting procedure reffered to as Approach 1 in the main text, the carboxylic acid head group and the hydrocarbon tail of the fatty acids are divided into separate layers. In addition, the headgroup layer is in contact with the a water (D_2O) backing, and the tail group is in contact with an air backing. The headgroup and tail SLDs are calculated from molecular dimensions. The thickness of the headgroup is calculated from surface excess measurments, and estimated to that of EA, also for 19-MEA, as this would represent maximum compression of the monolayer. Due to the low sensitivity of neutron to the aliphatic chain, the 19-MEA chain length was assumed to the extended chain length at the highest surface pressure and estimated to vary linearly with reduced molecular area. This estimation of the chain length agrees with the present data, and will be regarded as satisfactory for the purpose of this article. However, to receive a better estimation of the chain length it would be necessary to use a different contrast variation (deuterated chains), or use a probe more sensitive to hydrocarbon scattering (X-rays). The solvent penetration provides the relationship between the volume fraction of the headgroup and aliphatic tail of one molecule, and describes how much of the headgroup layer will be occupied by the underlaying solvent. At each interface (air–tails, tails–headgroups, and headgroups–water), a roughness parameter is added to account for capillary wave roughness in addition to the texturing of the monolayer (and the underlaying water). The only parameter used to fit the data using Approach 1, is the roughness parameter. This parameter is constrained to be identical for the three interfaces.

Approach 1 uses Motofit to generate a reflectivity curve using Equation 2 from the main text, and a SLD-profile using Equation 3. In Approach 2, the SLD-profile generated by Approach 1, was sliced into 30 slices of 3 Å thickness each. This provided an array of SLD-values corresponding to the average SLD-value at a certain distance from the interface, as modelled by Approach 1. These values were then imported into Motofit as 30 layers of 3 Å thickness, with no interfacial roughness, to generate a *new* reflectivity curve corresponding to reflectivity data using Equation 2. Additionally, a SLD-profile was generated as a step function to the newly loaded data, using Equation 3. Consequently, the SLD-profile and the curve corresponding to the reflectivity data were generated separately.

Supplementary discussion

S4 Roughness parameter in relation to capillary wave roughness

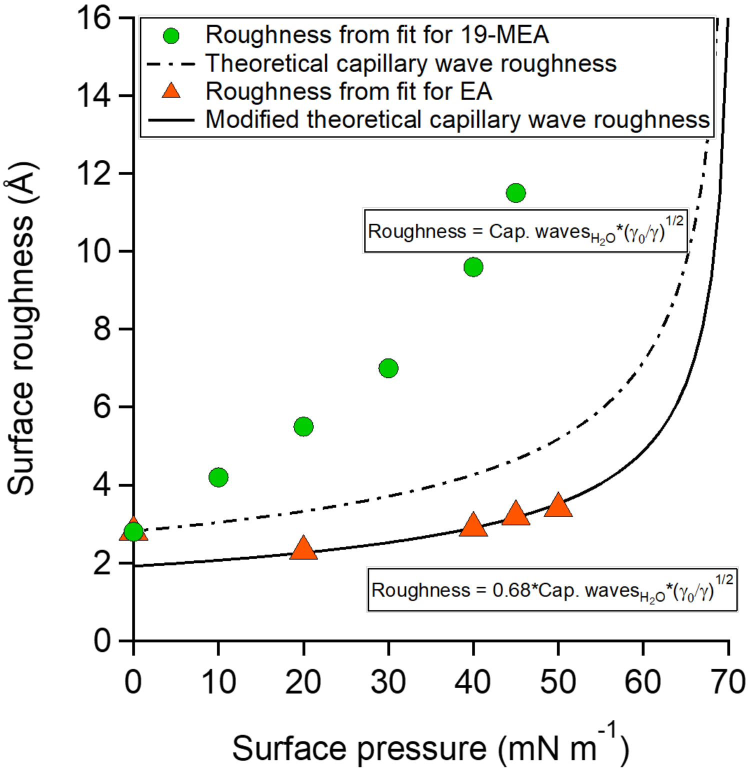

S4*. Variation of the surface roughness used to fit experimental NR data for 19-MEA (green circles) and EA (orange triangles) shown together with the theoretically expected increase in surface roughness due to thermally excited capillary waves of water (dashed line) with decreasing surface tension. Additionally, a modified version of the theoretical capillary wave roughness is shown (solid line) with a shift in surface roughness. The theoretical capillary wave roughness describes how the surface roughness perceived as thermally excited capillary waves changes as a function of surface tension, γ, where γ_0 is the surface tension of a neat water surface.*

Figure S4 shows the same data as Figure 4 in the article, with the addition of a shifted theoretical line for capillary waves. This shifted fit for thermally excited capillary waves overlap with the experimental fits for surface roughness for EA. This increase in surface pressure after an initial decrease (due to monolayer rigidity as the monolayer reaches a solid phase) is in agreement with what has been previously observed for behenic acid monolayers studied with X-ray reflectometry (59). Any attempts of a similar fit to the roughness for 19-MEA, yielded unsatisfactory results.

Estimation of number of fatty acid molecules per 19-MEA surface domain

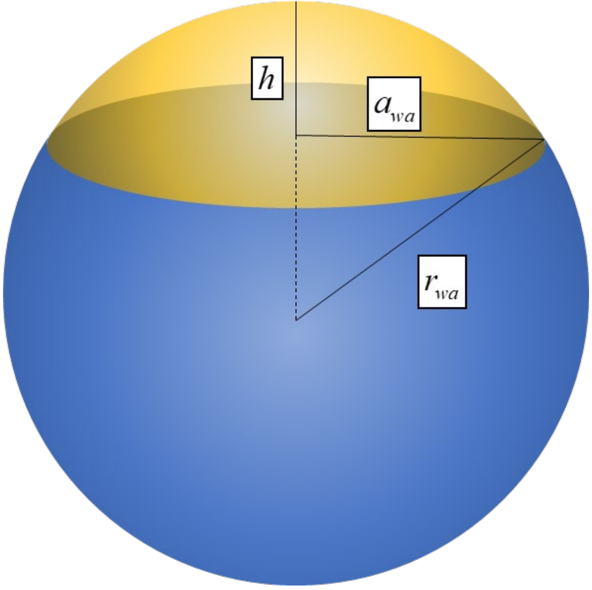

***S5.** Schematic representation of a spherical cap with parameters used to estimate the fatty acid coverage.*

A calculation of the number of molecules on a spherical cap is based on the radius of each aggregate extracted from AFM-images of deposited monolayers. This method yields 9575 molecules per aggregate employing a base radius of 250 Å and a cap height of 11.5 Å.

$$N_{MEA} = \frac{A_{cap}}{A_{EA}}$$

$$N_{MEA} = \frac{\pi\left(a_{wa}^2 + h^2\right)}{A_{EA}}$$

a_{wa} – base radius of spherical cap
h – height of spherical cap

The radius of curvature of the sphere can be calculated if the cap radius and height are known.

$$r_{cu} = \frac{\left(a_{wa}^2 + h^2\right)}{2h}$$

r_{cu} – radius of curvature of spherical cap

The radius of curvature can be calculated from molecular parameters using molecular parameters as described by reference (56):

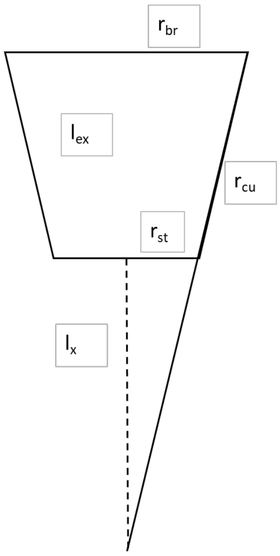

$$l_x = \frac{l_{ex}}{\left(\frac{r_{br}}{r_{st}} - 1\right)}$$

$$r_{cu} = \sqrt{\left(l_{ex} + l_x\right)^2 + r_{br}^2}$$

where r_{br} and r_{st} is the radius of the branched and straight chain radius, respectively, estimated from isotherm data at a desired surface pressure. An estimation based on reference (56) used the area per molecule values for EA and 19-MEA of 18.7 Å^2 and 19.1 Å^2, respectively, extracted from a surface pressure of 45 mN m^{-1}. The extended chain length was estimated to 25.6 Å for a C19 hydrocarbon chain, excluding the headgroup carbon.

References

56 Liljeblad JFD, Tyrode E, Thormann E, Dublanchet A-C, Luengo G, Magnus Johnson C, et al. *Phys Chem Chem Phys*, 2014, **16**, 17869–82.

57 Claesson PM, Berg JM. *Thin Solid Films*, 1989, **176**, 157–64.

58 Vollhardt D. Vols. 123–126, Advances in Colloid and Interface Science. 2006., p. 173–88.

59 Daillant J, Bosio L, Benattar JJ, Meunier J. *Europhys Lett*, 1989, **8**, 453–8.